
A 3D-CASCADING CROSSING COUPLING FRAMEWORK FOR HYPERCHAOTIC MAP CONSTRUCTION AND ITS APPLICATION TO COLOR IMAGE ENCRYPTION

Jilei Sun, Dianhong Wu

Department of Information Engineering

Shandong University of Aeronautics

Binzhou 256600, China

sunjilei@sdua.edu.cn, wudianhong@163.com

This work was supported by the Ph.D. Scientific Research Foundation of Shandong University of Aeronautics under Grant No. 801003023049.

ABSTRACT

This paper focuses on hyperchaotic-map construction and proposes a 3D-Cascading Crossing Coupling framework (3D-CCC), which cascades, crosses, and couples three one-dimensional chaotic maps to form a three-dimensional hyperchaotic system. The framework avoids modulo-1 operations and introduces bounded-state and denominator safeguards for stable digital implementation. A general 3D-CCC formulation is established, and its derivative/Jacobian structure is analyzed to characterize multidirectional expansion. By instantiating ICMIC, Logistic, and Sine maps, a concrete system (3D-ILS) is derived. Phase portraits, bifurcation behavior, sensitivity tests, and Lyapunov-exponent analysis indicate pronounced ergodicity and hyperchaotic dynamics. As an application of the constructed map, a one-round RGB image-encryption scheme is developed using cross-channel bit mixing with joint permutation-diffusion. Under the reported settings, the cipher reaches near-ideal entropy (average 7.9993), NPCR of 96.61%, UACI of 33.46%, and an effective key space of about 2^{309} . These results support the effectiveness of 3D-CCC as a practical framework for hyperchaotic-system design, with image encryption as one representative application.

Keywords Hyperchaotic Map · Image Encryption · 3D-CCC · Chaos

1 Introduction

With the rapid growth of Internet and mobile connectivity, the volume of data transmitted over networks has increased sharply, with images and videos accounting for a substantial share. In parallel, security breaches and privacy leaks have become more frequent, attracting sustained attention from governments, industry, and academia [1–3].

Chaotic image encryption is a widely studied approach for protecting visual data, leveraging the sensitivity to initial conditions and parameter perturbations exhibited by chaotic dynamical systems [4]. These properties are often exploited to generate pseudorandom sequences for permutation and diffusion, with the goal of reducing statistical structure in the ciphertext and increasing key sensitivity.

Motivated by the need for efficient yet security-oriented color image protection, this work focuses on constructing a practical hyperchaotic generator and using it to design a one-round RGB encryption algorithm. Specifically, we introduce a three-dimensional Cascading Crossing Coupling (3D-CCC) structure that combines three one-dimensional chaotic maps into a 3D hyperchaotic system. Based on 3D-CCC, we develop a new map termed 3D-ILS and use it to drive a fast color-image encryption procedure that performs cross-channel high/low-bit mixing together with permutation and diffusion in a single round. Experimental results indicate that the resulting scheme achieves strong security indicators, high efficiency, and robustness against common cryptanalytic tests.

The remainder of this paper is organized as follows. Section 2 reviews related work on chaos-based image encryption. Section 3 introduces the proposed 3D-CCC structure. Section 4 presents the construction of the 3D-ILS hyperchaotic map and analyzes its chaotic properties. Section 5 describes the color image encryption algorithm based on 3D-ILS. Section 6 reports simulation results and security performance analyses. Section 7 discusses limitations and practical considerations. Section 8 concludes the paper.

2 Related Work

Chaos-based image encryption has developed rapidly, particularly along directions such as high-dimensional chaotic systems, DNA-inspired coding, multi-chaotic frameworks, and cross-channel strategies for improving diffusion and statistical security. Recent studies commonly aim to enlarge the key space, increase key/plaintext sensitivity, and suppress residual correlation in encrypted color images.

2.1 Hybrid Chaotic and DNA-Enhanced Methods

A common direction is to combine chaotic dynamics with DNA coding to strengthen diffusion and increase combinatorial complexity. Wang et al. proposed a fast color image encryption method that integrates multi-chaotic systems with DNA operations, using three-dimensional permutation and global scrambling to reduce inter-pixel correlation and improve histogram uniformity [5].

2.2 Multi-Layered and Structural Enhancements

Layered chaotic constructions have also been explored to enhance confusion and diffusion. Guvenoglu introduced a multi-layer symmetric image-encryption scheme based on cascaded chaotic maps and reported improved resistance to differential attacks under standard evaluation protocols [6].

High-dimensional chaotic models are frequently analyzed for their dynamics and suitability in encryption. Zhao et al. developed an n -dimensional chaotic model and combined it with DNA-based algebraic operations to expand diffusion capability and provide flexible key-space design, supported by parameter-range analysis and randomness testing [7].

2.3 Cross-Channel and Fractal-Based Chaos Designs

To better exploit inter-channel dependencies in RGB images, several schemes integrate classical chaotic maps with additional structural mechanisms. For example, variable-structure discrete hyperchaotic systems have been used with cross-plane confusion and inter-channel mixing to improve security indicators relative to representative baselines [8].

Other approaches adopt discrete-space designs, such as hybrid chaotic maps coupled with three-dimensional cross-channel operations, to further disrupt pixel dependence. These methods typically report improvements in entropy and correlation metrics while maintaining resilience to common perturbations such as noise injection and cropping [9].

2.4 Foundational Survey and Systematic Analyses

Survey and review papers provide useful context for evaluation practices in chaotic image security. Singh et al. presented a systematic review of chaos-based image-security techniques, covering encryption, steganography, and watermarking, and discussing performance trade-offs and evaluation criteria [10].

Such surveys emphasize the importance of careful chaotic-system selection, consistent testing protocols, and attention to finite-precision effects that may degrade chaos in digital implementations. They also highlight the need for reproducible benchmarking to enable fair comparison across schemes.

2.5 Summary

Overall, recent work frequently combines multi-chaotic generators, symbolic operations (e.g., DNA coding), cross-channel mixing, and layered architectures to improve statistical security and key sensitivity. These directions motivate the present study, which targets a structured hyperchaotic construction and a single-round color-image encryption design.

3 3D-Cascading Crossing Coupling (3D-CCC) Structure

This paper proposes a three-dimensional Cascading Crossing Coupling (3D-CCC) structure that cascades, crosses, and couples three identical or distinct one-dimensional chaotic maps to form a 3D hyperchaotic system. Relative to one-dimensional maps and many two-dimensional constructions, 3D hyperchaotic systems can exhibit richer dynamics that may benefit security-oriented sequence generation. The added dynamical complexity may increase computational cost; therefore, practical use should balance security requirements against efficiency constraints.

Many existing constructions rely on modulo-1 operations [11–14]. In contrast, the proposed 3D-CCC formulation avoids modulo operations, which simplifies implementation and can reduce error accumulation due to finite-precision arithmetic, improving numerical stability.

The 3D-CCC coupling rule for constructing a higher-dimensional hyperchaotic system from three one-dimensional maps is defined as follows.

Let F , G , and H be three one-dimensional chaotic maps defined on $(0, 1)$. Specifically, we adopt:

$$F(u) = \frac{1}{2} \left[\sin \left(\frac{\alpha}{2u-1} \right) + 1 \right], \quad (1)$$

$$G(u) = ru(1-u), \quad 0 < r \leq 4, \quad (2)$$

$$H(u) = \frac{1}{2} [\sin(\mu\pi(2u-1)) + 1]. \quad (3)$$

To keep the state within $(0, 1)$ without introducing modulo operations, we define the saturation operator:

$$\text{sat}(u) = \min(1 - \varepsilon, \max(\varepsilon, u)), \quad (4)$$

where ε is a small positive constant. In numerical implementation, the singular denominator in $F(u)$ is also protected by

$$\text{den}(u) = \begin{cases} 2u-1, & |2u-1| \geq \varepsilon_d, \\ \text{sgn}(2u-1) \varepsilon_d, & |2u-1| < \varepsilon_d, \end{cases}$$

which avoids division by values too close to zero.

The 3D-CCC system is then defined as:

$$\begin{cases} u_1 = x_n G(y_n) + (1-x_n)H(z_n) + c(y_n - z_n) \left(x_n - \frac{1}{2}\right), \\ x_{n+1} = F(\text{sat}(u_1)), \\ u_2 = y_n G(z_n) + (1-y_n)H(x_{n+1}) + c(z_n - x_{n+1}) \left(y_n - \frac{1}{2}\right), \\ y_{n+1} = F(\text{sat}(u_2)), \\ u_3 = z_n G(x_{n+1}) + (1-z_n)H(y_{n+1}) + c(x_{n+1} - y_{n+1}) \left(z_n - \frac{1}{2}\right), \\ z_{n+1} = F(\text{sat}(u_3)). \end{cases} \quad (5)$$

Here, c is a small coupling coefficient controlling the intensity of cross-variable interactions.

In (5), the variables x , y , and z denote the three-dimensional sequences generated by the 3D-CCC structure. A schematic overview of the coupling architecture is shown in Figure 1.

4 Construction and Analysis of the 3D-ILS Hyperchaotic Map

4.1 Formulation of the 3D-ILS Hyperchaotic Map

To construct the 3D-ILS hyperchaotic system, we instantiate the 3D-CCC framework by choosing the ICMIC map [15] as F , the Logistic map [16] as G , and the Sine map [17] as H . To enable effective cascading and coupling, inputs and outputs are normalized to $(0, 1)$. The normalized iterations of the Sine, Logistic, and ICMIC maps are given in (6)–(8).

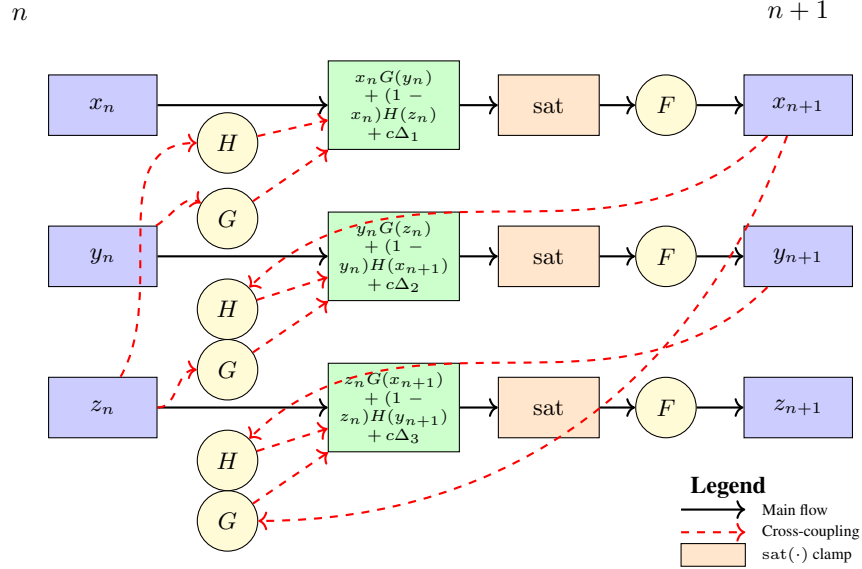


Figure 1: 3D-CCC structure constructed from three cross-coupled 1-D maps. The diagram explicitly includes the additive coupling terms $c\Delta_i$ and the $\text{sat}(\cdot)$ clamp before each F block.

$$x_{n+1} = \frac{1}{2} [\sin(\mu\pi(2x_n - 1)) + 1] \quad (6)$$

$$x_{n+1} = rx_n(1 - x_n) \quad (7)$$

$$x_{n+1} = \frac{1}{2} \left[\sin\left(\frac{\alpha}{2x_n - 1}\right) + 1 \right] \quad (8)$$

By substituting the above three equations into Equation 5, the iterative form of the 3D-ILS hyperchaotic map is obtained, as shown in Equation 9.

$$\begin{cases} u_1 = \text{sat}\left(x_n(r y_n(1 - y_n)) + (1 - x_n) \frac{\sin(\mu\pi(2z_n - 1)) + 1}{2} + c(y_n - z_n)(x_n - \frac{1}{2})\right), \\ x_{n+1} = \frac{1}{2} \left[\sin\left(\frac{\alpha}{\text{den}(u_1)}\right) + 1 \right], \\ u_2 = \text{sat}\left(y_n(r z_n(1 - z_n)) + (1 - y_n) \frac{\sin(\mu\pi(2x_{n+1} - 1)) + 1}{2} + c(z_n - x_{n+1})(y_n - \frac{1}{2})\right), \\ y_{n+1} = \frac{1}{2} \left[\sin\left(\frac{\alpha}{\text{den}(u_2)}\right) + 1 \right], \\ u_3 = \text{sat}\left(z_n(r x_{n+1}(1 - x_{n+1})) + (1 - z_n) \frac{\sin(\mu\pi(2y_{n+1} - 1)) + 1}{2} + c(x_{n+1} - y_{n+1})(z_n - \frac{1}{2})\right), \\ z_{n+1} = \frac{1}{2} \left[\sin\left(\frac{\alpha}{\text{den}(u_3)}\right) + 1 \right]. \end{cases} \quad (9)$$

Unless otherwise stated, the coupling coefficient is fixed to $c = c_0 = 0.077$ in all experiments.

4.2 Jacobian Matrix and Derivative Structure

Let $\mathbf{s}_n = (x_n, y_n, z_n)^\top$ and $\mathbf{s}_{n+1} = T(\mathbf{s}_n)$, where T is defined by Equation 5. For compact notation, define

$$\Phi(v) = \frac{1}{2} \left[\sin\left(\frac{\alpha}{\text{den}(v)}\right) + 1 \right], \quad F(v) = \Phi(\text{sat}(v)).$$

Then

$$x_{n+1} = F(u_1), \quad y_{n+1} = F(u_2), \quad z_{n+1} = F(u_3).$$

The derivatives of the primitive maps are

$$G'(u) = r(1 - 2u), \quad H'(u) = \mu\pi \cos(\mu\pi(2u - 1)). \quad (10)$$

For the safeguarded singular denominator and saturation operator, we use

$$\text{den}'(v) = \begin{cases} 2, & |2v - 1| \geq \varepsilon_d, \\ 0, & |2v - 1| < \varepsilon_d, \end{cases} \quad \text{sat}'(u) = \begin{cases} 1, & \varepsilon < u < 1 - \varepsilon, \\ 0, & \text{otherwise.} \end{cases} \quad (11)$$

Hence

$$\Phi'(v) = -\frac{\alpha \cos(\alpha/\text{den}(v))}{\text{den}(v)^2} \text{den}'(v), \quad F'(u) = \Phi'(\text{sat}(u)) \text{sat}'(u). \quad (12)$$

Let $M_i = F'(u_i)$ for $i = 1, 2, 3$. For u_1 ,

$$\begin{aligned} \frac{\partial u_1}{\partial x_n} &= G(y_n) - H(z_n) + c(y_n - z_n), \\ \frac{\partial u_1}{\partial y_n} &= x_n G'(y_n) + c\left(x_n - \frac{1}{2}\right), \\ \frac{\partial u_1}{\partial z_n} &= (1 - x_n)H'(z_n) - c\left(x_n - \frac{1}{2}\right), \end{aligned} \quad (13)$$

and

$$\frac{\partial x_{n+1}}{\partial \xi} = M_1 \frac{\partial u_1}{\partial \xi}, \quad \xi \in \{x_n, y_n, z_n\}. \quad (14)$$

For u_2 , define $A_2 = (1 - y_n)H'(x_{n+1}) - c(y_n - \frac{1}{2})$, then

$$\begin{aligned} \frac{\partial u_2}{\partial x_n} &= A_2 \frac{\partial x_{n+1}}{\partial x_n}, \\ \frac{\partial u_2}{\partial y_n} &= G(z_n) - H(x_{n+1}) + c(z_n - x_{n+1}) + A_2 \frac{\partial x_{n+1}}{\partial y_n}, \\ \frac{\partial u_2}{\partial z_n} &= y_n G'(z_n) + c\left(y_n - \frac{1}{2}\right) + A_2 \frac{\partial x_{n+1}}{\partial z_n}, \end{aligned} \quad (15)$$

and

$$\frac{\partial y_{n+1}}{\partial \xi} = M_2 \frac{\partial u_2}{\partial \xi}, \quad \xi \in \{x_n, y_n, z_n\}. \quad (16)$$

For u_3 , define

$$B_x = z_n G'(x_{n+1}) + c\left(z_n - \frac{1}{2}\right), \quad B_y = (1 - z_n)H'(y_{n+1}) - c\left(z_n - \frac{1}{2}\right),$$

then

$$\begin{aligned} \frac{\partial u_3}{\partial x_n} &= B_x \frac{\partial x_{n+1}}{\partial x_n} + B_y \frac{\partial y_{n+1}}{\partial x_n}, \\ \frac{\partial u_3}{\partial y_n} &= B_x \frac{\partial x_{n+1}}{\partial y_n} + B_y \frac{\partial y_{n+1}}{\partial y_n}, \\ \frac{\partial u_3}{\partial z_n} &= G(x_{n+1}) - H(y_{n+1}) + c(x_{n+1} - y_{n+1}) + B_x \frac{\partial x_{n+1}}{\partial z_n} + B_y \frac{\partial y_{n+1}}{\partial z_n}, \end{aligned} \quad (17)$$

and

$$\frac{\partial z_{n+1}}{\partial \xi} = M_3 \frac{\partial u_3}{\partial \xi}, \quad \xi \in \{x_n, y_n, z_n\}. \quad (18)$$

Therefore the Jacobian matrix is

$$J_n = \frac{\partial(x_{n+1}, y_{n+1}, z_{n+1})}{\partial(x_n, y_n, z_n)} = \begin{bmatrix} \partial_{x_n} x_{n+1} & \partial_{y_n} x_{n+1} & \partial_{z_n} x_{n+1} \\ \partial_{x_n} y_{n+1} & \partial_{y_n} y_{n+1} & \partial_{z_n} y_{n+1} \\ \partial_{x_n} z_{n+1} & \partial_{y_n} z_{n+1} & \partial_{z_n} z_{n+1} \end{bmatrix}. \quad (19)$$

4.3 Possibility of Three Positive Lyapunov Exponents

Let $\sigma_1(J_n) \geq \sigma_2(J_n) \geq \sigma_3(J_n) > 0$ be the singular values of J_n . For finite-time exponents over N steps, one has

$$\lambda_i^{(N)} = \frac{1}{N} \sum_{n=0}^{N-1} \log \sigma_i(J_n), \quad i = 1, 2, 3, \quad (20)$$

and

$$\sum_{i=1}^3 \lambda_i^{(N)} = \frac{1}{N} \sum_{n=0}^{N-1} \log |\det J_n|. \quad (21)$$

Because $F'(u)$ contains the factor $\alpha/\text{den}(\text{sat}(u))^2$, the local expansion rate can be strongly amplified when trajectories approach the safeguarded singular surface. Meanwhile, the cross-coupling coefficient c introduces nontrivial off-diagonal terms in J_n , which helps maintain full-rank directional mixing instead of one-directional stretching.

A sufficient condition for three positive Lyapunov exponents is

$$\liminf_{N \rightarrow \infty} \frac{1}{N} \sum_{n=0}^{N-1} \log \sigma_3(J_n) > 0. \quad (22)$$

Under this condition, $\lambda_3 > 0$, and since $\lambda_1 \geq \lambda_2 \geq \lambda_3$, all three exponents are positive. For the proposed 3D-CCC form, this condition is achievable for suitable (α, r, μ) with fixed $c = c_0$, because:

$$\sigma_3(J_n) \text{ can be lifted above } 1 \quad (23)$$

by the combined effect of singular amplification (F') and cross-directional coupling (off-diagonal Jacobian terms), while the saturation and denominator safeguards keep the orbit bounded and numerically stable. Therefore, the model is theoretically capable of exhibiting three positive Lyapunov exponents.

The 3D-ILS map exhibits pronounced chaotic behavior over a wide range of control-parameter combinations (α, r, μ) under fixed c_0 . Figure 2 shows representative phase portraits for selected parameter sets, using the initial condition $(x_0, y_0, z_0) = (0.3, 0.3, 0.3)$.

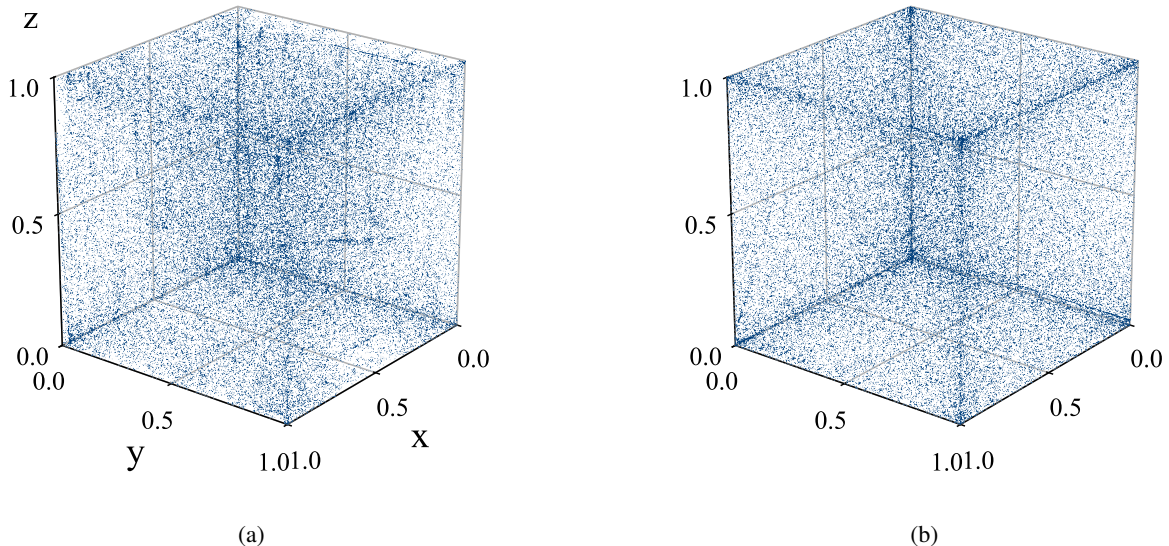


Figure 2: 3D phase space diagrams of the 3D-ILS map under different parameter sets with the same initial condition $(x_0, y_0, z_0) = (0.3, 0.3, 0.3)$. Parameter settings are: (a) $(\alpha = 5.2, r = 3.7, \mu = 8.3)$, and (b) $(\alpha = 58.4, r = 3.8, \mu = 11.1)$, with fixed $c = c_0$.

As shown in Figure 2, for most tested parameter combinations, trajectories densely occupy the unit cube and display a relatively uniform spatial distribution. This indicates strong ergodicity and supports the suitability of 3D-ILS for pseudorandom sequence generation.

4.4 Bifurcation Diagram

The 3D-ILS map involves three state variables (x, y, z) and three control parameters α , r , and μ , while c is fixed as c_0 . Let the default values of the scanned parameters be $\alpha = 10$, $r = 4$, and $\mu = 5$. To analyze the influence of each control parameter on the system's dynamics, we vary one parameter while keeping the other two fixed at their default values. For each setting, the system is iterated 1,000 times, and the resulting values of (x, y, z) are recorded. By repeating this process over a range of parameter values, the evolution of the state variables with respect to each control parameter can be visualized through bifurcation diagrams, as shown in Figure 3.

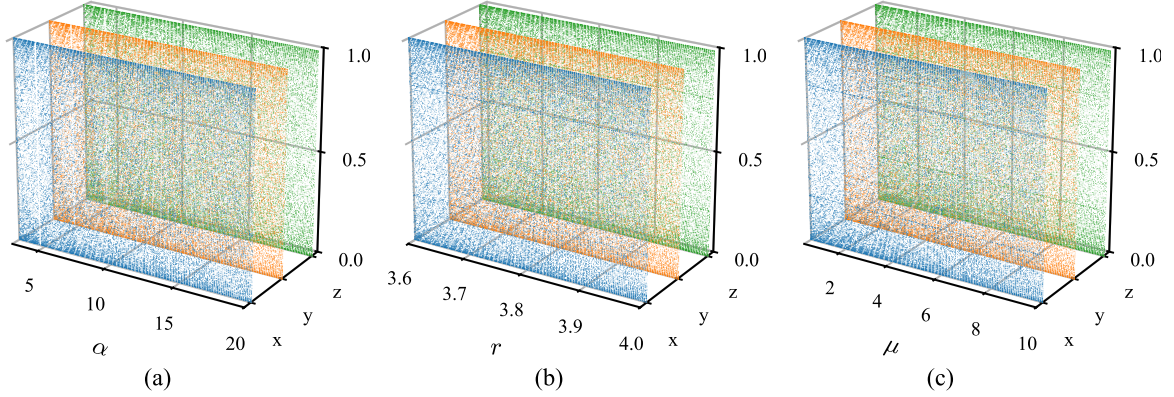


Figure 3: Bifurcation diagrams of the 3D-ILS map. In each panel, the three state variables are stacked as three layers on the middle axis (labeled as x , y , and z). The control parameters varied in each panel are: (a) α with $r = 4$ and $\mu = 5$, (b) r with $\alpha = 10$ and $\mu = 5$, and (c) μ with $\alpha = 10$ and $r = 4$. In all panels, $c = c_0$.

4.5 Sensitivity Analysis

One of the fundamental characteristics of chaotic systems is their sensitivity to initial conditions. When starting from two nearby initial points that differ only slightly, this minute difference is continuously amplified through iterations, eventually resulting in completely divergent trajectories.

To evaluate sensitivity to initial conditions, we set $\alpha = 10$, $r = 4$, $\mu = 5$, and $c = c_0$. Two neighboring initial states are selected as $\mathbf{p}_0 = (x_0, y_0, z_0)$ and $\mathbf{p}_1 = (x_0 + \delta, y_0 + \delta, z_0 + \delta)$, with $x_0 = y_0 = z_0 = 0.3$ and $\delta = 10^{-16}$. Each state is iterated 50 times, and the resulting x , y , and z sequences are recorded (Figure 4).

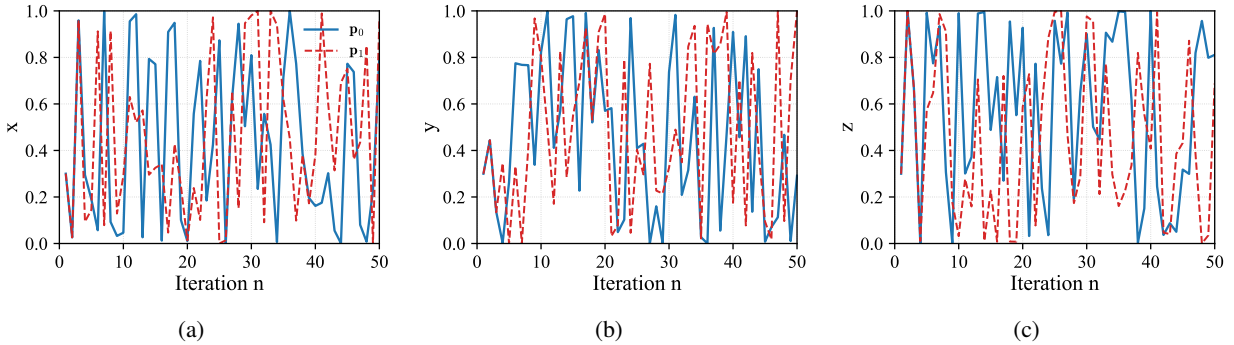


Figure 4: Sensitivity to initial conditions of the 3D-ILS system with $\alpha = 10$, $r = 4$, $\mu = 5$, and fixed $c = c_0$. Trajectories of two adjacent initial states diverge rapidly over 50 iterations. (a) x coordinate, (b) y coordinate, and (c) z coordinate.

Figure 4 shows that, despite an extremely small perturbation, the trajectories separate rapidly; clear divergence is visible on all three axes within a few iterations. The coordinate differences then evolve irregularly, consistent with

strong sensitivity to initial conditions. Similar behavior is observed across additional randomly sampled neighboring initial states, further supporting this conclusion.

4.6 Lyapunov Exponents

For the 3D-ILS map, Lyapunov exponents were computed by QR-based evolution of tangent vectors, where the Jacobian at each step is obtained by finite-difference differentiation of the safeguarded map in Equation 9. The initial condition is $(x_0, y_0, z_0) = (0.31, 0.37, 0.41)$, and $c = c_0$ is fixed. The results are shown in Figure 5.

The three panels sweep α , r , and μ around the reference parameter set $(\alpha, r, \mu) = (74.7631, 3.8647, 11.3289)$. In these sweeps, two to three Lyapunov exponents remain positive, and broad regions satisfy $\lambda_3 > 0$, indicating hyperchaotic dynamics. Moreover, a constructive search identifies one explicit parameter set with three positive exponents:

$$(\alpha, r, \mu) = (109.1686, 3.9570, 14.4175),$$

with

$$(\lambda_1, \lambda_2, \lambda_3) = (14.429966, 12.450648, 3.100630).$$

This numerical evidence is consistent with the Jacobian- and singular-value-based analysis presented above.

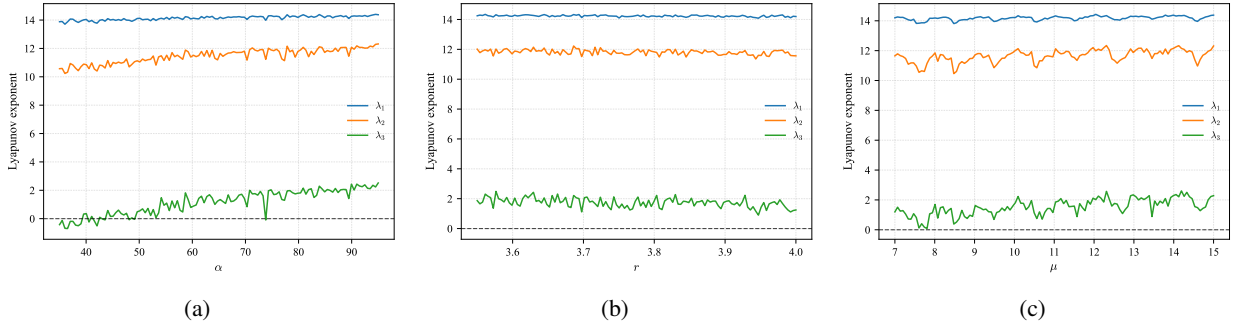


Figure 5: Lyapunov exponent curves of the 3D-ILS map computed by finite-difference Jacobian and QR iteration. Initial state: $x_0 = 0.31$, $y_0 = 0.37$, $z_0 = 0.41$, with fixed $c = c_0$. (a) LEs vs α with fixed $r = 3.8647$, $\mu = 11.3289$. (b) LEs vs r with fixed $\alpha = 74.7631$, $\mu = 11.3289$. (c) LEs vs μ with fixed $\alpha = 74.7631$, $r = 3.8647$.

5 Color Image Encryption Based on 3D-ILS with RGB Channel Bit-Level Mixing

This section presents a color image encryption algorithm based on the 3D-ILS hyperchaotic map. The proposed method integrates RGB channel data at the bit level and performs simultaneous permutation and diffusion, enabling strong encryption performance in a single round. The overall framework of the algorithm is illustrated in Figure 6.

5.1 Key Generation from Plaintext

The encryption keys are derived from the plaintext image, improving plaintext sensitivity and reducing key reuse across different images. Specifically, six parameters are generated from the image content: three control parameters (α, r, μ) and three initial values (x_0, y_0, z_0) . The key-generation mechanism is summarized in Figure 7. The coupling coefficient is fixed at $c = c_0$ and is not treated as a key parameter.

The key generation process, formalized in Algorithm 1, computes a 256-bit hash $h = \text{SHA256}(P)$ partitioned into 16 segments of 16 bits each, with bitwise operations applied to derive 18 auxiliary values. These values are

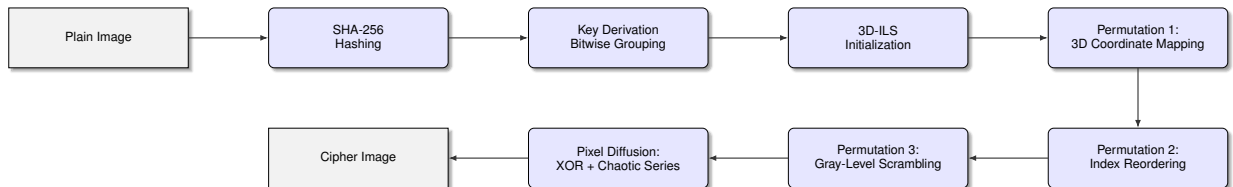


Figure 6: Framework of the proposed image encryption algorithm.

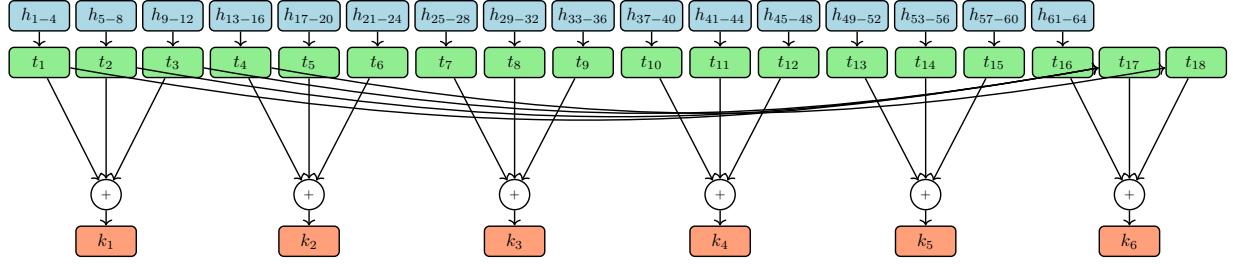


Figure 7: Key generation mechanism from plaintext image.

Algorithm 1: Key Generation from Plaintext

Input: Plaintext image P

Output: Chaotic parameters α, r, μ and initial values x_0, y_0, z_0

- 1 $h \leftarrow \text{SHA256}(P)$, $|h| = 256$ bits (64 hexadecimal characters)
 - 2 $h \leftarrow [h_1 \| h_2 \| \dots \| h_{16}]$, $h_j \in \{0, 1\}^{16}$
 - 3 $t_j \leftarrow \text{dec}(h_j)$, $j = 1, \dots, 16$
 - 4 $t_{17} \leftarrow t_1 \wedge t_2 \oplus t_3$
 - 5 $t_{18} \leftarrow t_4 \wedge t_5 \oplus t_6$
 - 6 $k_i \leftarrow \left(\sum_{j=1}^3 t_{3(i-1)+j} \right) \bmod 2^{16}$, $i = 1, \dots, 6$
 - 7 $\tilde{k}_i \leftarrow k_i / 2^{16}$
 - 8 $\alpha \leftarrow 3 + 3\tilde{k}_1$, $r \leftarrow 3.7 + 0.3\tilde{k}_2$, $\mu \leftarrow 5 + 5\tilde{k}_3$
 - 9 $x_0 \leftarrow \tilde{k}_4$, $y_0 \leftarrow \tilde{k}_5$, $z_0 \leftarrow \tilde{k}_6$
-

aggregated into six normalized parameters $\tilde{k}_i \in [0, 1)$, which are then mapped via affine transformations to the chaotic system parameters (α, r, μ) and initial conditions (x_0, y_0, z_0) . The coupling coefficient is fixed at $c = c_0$.

5.2 Cross-Channel Bit-Level Mixing

Let $(R, G, B) \in \mathbb{Z}_8^{h \times w \times 3}$ denote the plaintext RGB image. Each channel is decomposed as

$$R = R_H \| R_L, \quad G = G_H \| G_L, \quad B = B_H \| B_L,$$

where $R_H, R_L \in \mathbb{Z}_4^{h \times w}$ denote the high and low nibbles, respectively. The bit-level mixing stage defines an invertible linear transformation T that maps $(R_H, R_L, G_H, G_L, B_H, B_L)$ to (R_{en}, G_{en}, B_{en}) by

$$(R_{en}, G_{en}, B_{en}) = (G_L \| B_H, B_L \| R_H, R_L \| G_H).$$

Invertibility follows directly from the explicit inverse mapping T^{-1} .

5.3 Combined Pixel Permutation and Diffusion

For the bit-mixed image $Q \in \mathbb{Z}_8^{h \times w \times 3}$ with $n = hw$ pixels, three chaotic orbits $X, Y, Z \in \mathbb{R}^n$ are generated by the 3D-ILS map and concatenated into $U \in \mathbb{R}^{3n}$. Sorting U yields a permutation W used for pixel reordering. In parallel, U is quantized to $V \in \mathbb{Z}_8^{3n}$ via $V_i = \lfloor 10000U_i \rfloor \wedge 255$. Permutation and diffusion are then performed as specified in Algorithm 2, using XOR-based feedback diffusion to ensure that each output depends on the chaotic sequence, permutation indices, and prior ciphertext elements.

5.4 Decryption

Decryption reverses these operations by regenerating the same chaotic sequences and applying inverse diffusion and inverse permutation in reverse order. Given the cipher image $C \in \mathbb{Z}_8^{h \times w \times 3}$, the algorithm first recovers the bit-mixed image Q by inverting the recurrence in Algorithm 3, and then applies T^{-1} to reconstruct the plaintext image.

Algorithm 2: Permutation and Diffusion

Input: Bit-mixed image $Q \in \mathbb{Z}_8^{h \times w \times 3}$, $n = h \cdot w$
Output: Encrypted image $C \in \mathbb{Z}_8^{3n}$

- 1 $[X, Y, Z] \leftarrow \text{3D-ILS}(\alpha, r, \mu, c_0, x_0, y_0, z_0, n)$
- 2 $U \leftarrow [X \| Y \| Z] \in \mathbb{R}^{3n}$
- 3 $W \leftarrow \text{argsort}(U)$
- 4 $V \leftarrow (\lfloor 10000 \cdot U \rfloor \wedge 255) \in \mathbb{Z}_8^{3n}$
- 5 $R \leftarrow \text{vec}(Q) \in \mathbb{Z}_8^{3n}$
- 6 $D(1) \leftarrow R(W(1)) \oplus R(W(3n)) \oplus R(W(3n-1)) \oplus V(1)$
- 7 **for** $i = 2$ **to** $3n$ **do**
- 8 **if** $i \equiv 2 \pmod{2}$ **then**
- 9 $D(i) \leftarrow R(W(i)) \oplus D(i-1) \oplus R(W(3n)) \oplus V(i)$
- 10 **else**
- 11 $D(i) \leftarrow R(W(i)) \oplus D(i-1) \oplus D(i-2) \oplus V(i)$
- 12 $C \leftarrow \text{reshape}(D, h \times w \times 3)$

Algorithm 3: Decryption

Input: Cipher image $C \in \mathbb{Z}_8^{3n}$, keys $(\alpha, r, \mu, x_0, y_0, z_0)$
Output: Plaintext image P

- 1 $[X, Y, Z] \leftarrow \text{3D-ILS}(\alpha, r, \mu, c_0, x_0, y_0, z_0, n)$
- 2 $U \leftarrow [X \| Y \| Z]$
- 3 $W \leftarrow \text{argsort}(U)$
- 4 $V \leftarrow (\lfloor 10000 \cdot U \rfloor \wedge 255)$
- 5 $D \leftarrow \text{vec}(C) \in \mathbb{Z}_8^{3n}$
- 6 **for** $i = 3n$ **to** 3 **step** -1 **do**
- 7 $R(W(i)) \leftarrow D(i) \oplus D(i-1) \oplus D(i-2) \oplus V(i)$
- 8 $R(W(2)) \leftarrow D(2) \oplus D(1) \oplus R(W(3n)) \oplus V(2)$
- 9 $R(W(1)) \leftarrow D(1) \oplus R(W(3n)) \oplus R(W(3n-1)) \oplus V(1)$
- 10 $Q \leftarrow \text{reshape}(R, h \times w \times 3)$
- 11 $P \leftarrow \text{BitMix}^{-1}(Q)$

6 Simulation and Security Performance Analysis

This section reports experimental results and evaluates the proposed encryption algorithm in terms of statistical security indicators and robustness under common test settings.

6.1 Experimental Setup

Unless otherwise specified, all experiments were conducted on a standard desktop computer. The test images are 8-bit RGB images, and all reported results correspond to the three color channels. For chaotic sequence generation, the system was iterated for a sufficient number of steps, and initial transient iterations were discarded to reduce initialization bias. The coupling coefficient was fixed as $c = c_0$ in all experiments. The statistical metrics reported in this section (entropy, correlation coefficients, NPCR, and UACI) follow their standard definitions and are computed on the cipher images produced by the proposed scheme.

6.2 Simulation Results

To verify correctness, three benchmark images (Airplane, House, and Peppers) are encrypted and decrypted (Figure 8). The ciphertext images appear visually noise-like, whereas decryption with the correct key recovers the plaintext images exactly, confirming reversibility.

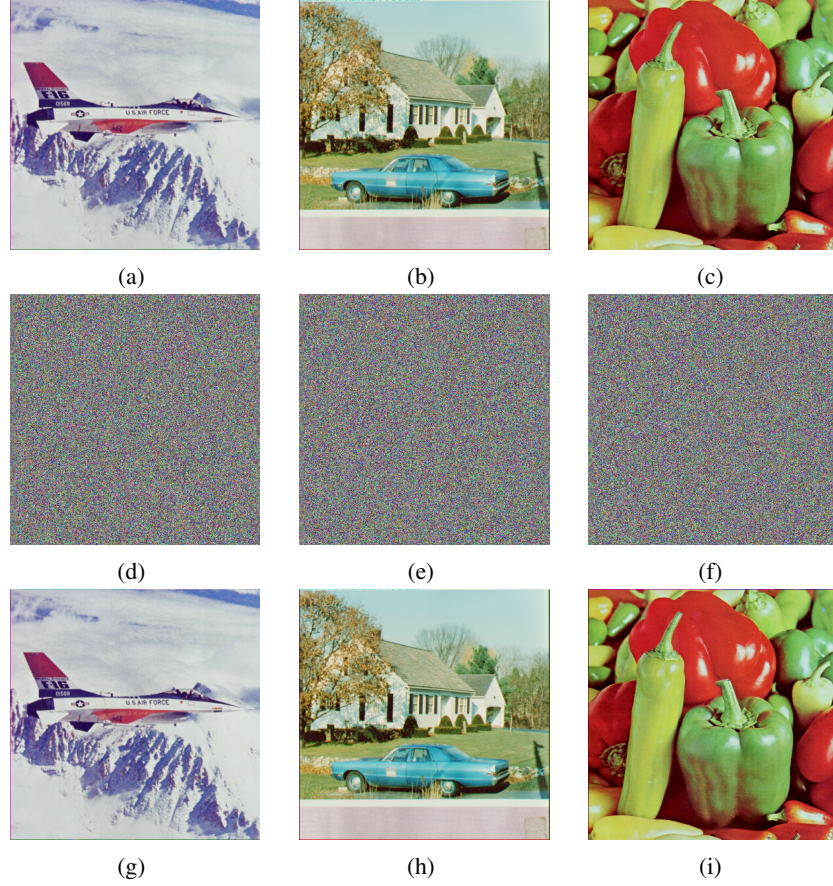


Figure 8: Simulation results of the proposed image encryption algorithm. (a) Airplane plaintext; (b) House plaintext; (c) Peppers plaintext; (d) Encrypted Airplane; (e) Encrypted House; (f) Encrypted Peppers; (g) Decrypted Airplane; (h) Decrypted House; (i) Decrypted Peppers.

6.3 Key Sensitivity Analysis

A secure encryption scheme should be highly sensitive to the secret key: a one-bit change in any key component should produce a substantially different ciphertext. To evaluate this property, four perturbed keys $K1-K4$ are generated by flipping a single bit of the original 256-bit key $K0$, as listed below (modified bits highlighted in red).

$K0 = 26DC1686AA460F215375FE0B468F6F4BD45D067B81BF4BBCF3D73BED5CC1BBD3$
 $K1 = 26DC1686AA460F215375FE0B468F6F4BD45D067B81BF4BBCF3D73BED5CC1BBD2$
 $K2 = 26DC1686AA460F215375FE0B468F6F4BD45D067B81BF4BBCF3D73BED5CC1BBE3$
 $K3 = 26DC1686AA460F215375FE0B468F6F4BD45D067B81BF4BBCF3D73BED5CC1BAD3$
 $K4 = 26DC1686AA460F215375FE0B468F6F4BD45D067B81BF4BBCF3D73BED5CC1CBD3$

Each perturbed key yields a visually distinct ciphertext, and decryption under an incorrect key fails, producing noise-like outputs. Histogram comparisons further support strong key sensitivity (Figure 9).

6.4 Information Entropy Analysis

Information entropy measures randomness in the encrypted image. For 8-bit imagery, the ideal entropy is 8. The proposed algorithm produces entropy values close to 8 across all three RGB channels. Table 1 compares these results with recent methods.

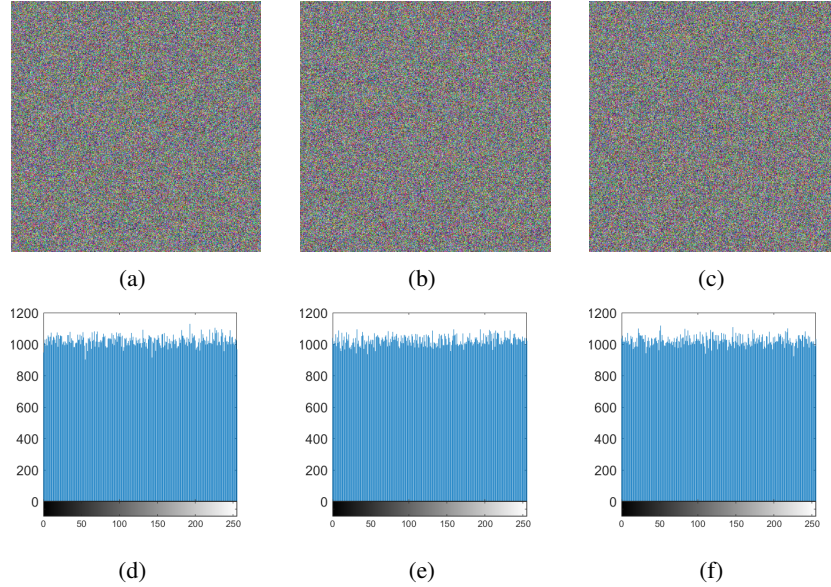


Figure 9: Key sensitivity analysis: Decrypted images and their histograms using similar but wrong keys. (a) Decrypted with $K1$; (b) Decrypted with $K2$; (c) Decrypted with $K3$; (d) Histogram with $K1$; (e) Histogram with $K2$; (f) Histogram with $K3$.

Table 1: Comparison of Information Entropy

Algorithm	Red	Green	Blue	Average
Proposed	7.9993	7.9993	7.9993	7.9993
Ref. [18]	7.9972	7.9972	7.9970	7.9971
Ref. [19]	7.9993	7.9993	7.9993	7.9993
Ref. [20]	7.9991	7.9993	7.9993	7.9992
Ref. [21]	7.9993	7.9992	7.9992	7.9992
Ref. [22]	7.9964	7.9984	7.9961	7.9970

6.5 Key Space Analysis

Resistance to brute-force search requires a sufficiently large key space. The proposed scheme uses six 64-bit real-valued parameters, corresponding to an effective key space of approximately 2^{309} , which exceeds the commonly cited 2^{100} threshold. Table 2 summarizes the comparison with representative approaches.

Table 2: Key Space Comparison

Algorithm	Proposed	Ref. [23]	Ref. [24]	Ref. [25]	Ref. [26]	Ref. [27]
Key Space Size	2^{309}	2^{256}	2^{256}	2^{305}	2^{215}	2^{287}

Note: values are reported as key-space cardinality in exponential form.

6.6 Correlation Analysis

Natural images exhibit strong local correlation among adjacent pixels; effective encryption should reduce this correlation toward zero. Figure 10 shows adjacent-pixel distributions in the horizontal, vertical, and diagonal directions for the plaintext and ciphertext. Table 3 reports the corresponding correlation coefficients for each RGB channel, demonstrating substantial decorrelation.

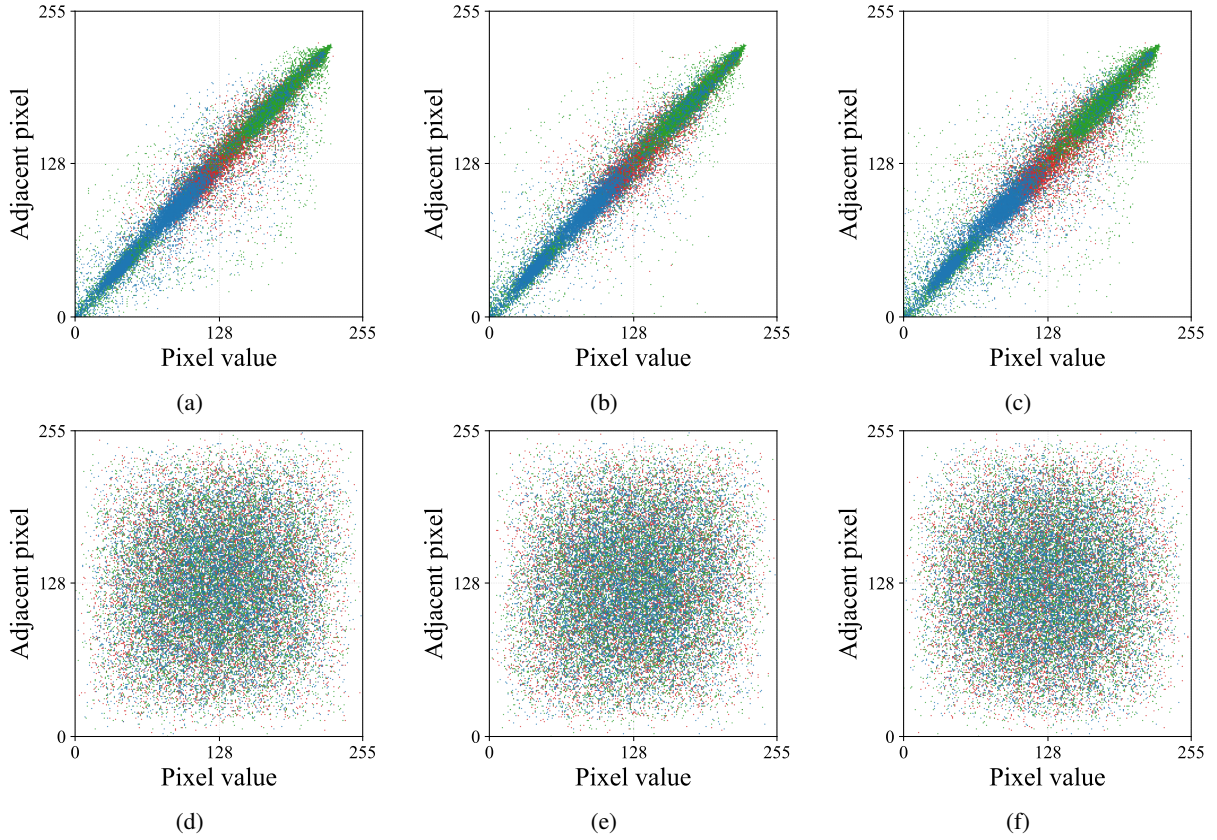


Figure 10: Correlation analysis of adjacent pixels in plain and cipher images. (a) Plain image, horizontal direction; (b) Plain image, vertical direction; (c) Plain image, diagonal direction; (d) Cipher image, horizontal direction; (e) Cipher image, vertical direction; (f) Cipher image, diagonal direction.

Table 3: Comparison of Correlation Coefficients

Algorithm	Direction	R	G	B
Proposed	H	0.0007	-0.005	0.0005
	V	-0.009	-0.0025	0.0010
	D	0.0028	-0.0031	0.0010
Ref. [28]	-	0.0031	0.0031	0.0031
Ref. [29]	-	-0.0038	-0.0038	-0.0038
Ref. [30]	-	0.0130	0.0141	-0.0258
Ref. [31]	-	0.0012	0.0006	0.0021
Ref. [32]	-	-0.0319	-0.0140	0.0065

Note: H, V, and D denote horizontal, vertical, and diagonal directions, respectively.

6.7 Differential Attack Resistance

Differential attack is a common cryptanalytic technique in which an attacker encrypts two plaintext images that differ by only a single pixel and analyzes the differences between the resulting cipher images to identify exploitable patterns. A secure encryption algorithm should exhibit strong diffusion properties, such that even a minimal change in the plaintext – such as a one-pixel variation – results in significant and unpredictable changes across the entire cipher image. This ensures that no meaningful correlation can be inferred by the attacker.

To evaluate resistance to differential attacks, we modify one pixel in the *Peppers* image to obtain a slightly altered version. Both images are encrypted under the same key, producing ciphertexts C_1 and C_2 . The absolute difference image D_{12} is computed as the pixel-wise absolute difference between C_1 and C_2 . As shown in Figure 11, differences spread across the ciphertext, indicating strong diffusion and resistance to differential analysis.

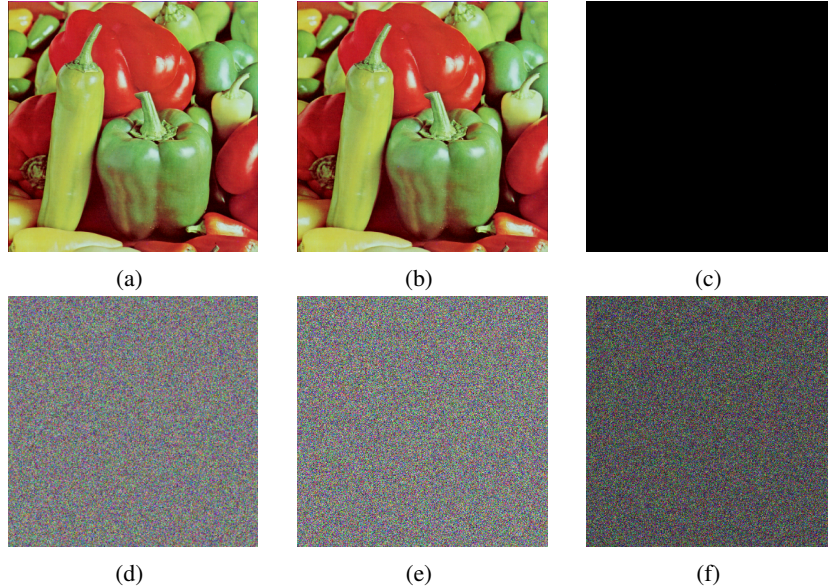


Figure 11: Differential analysis of the proposed encryption algorithm. (a) Original image; (b) Modified image; (c) Absolute difference image; (d) Cipher image C_1 ; (e) Cipher image C_2 ; (f) Absolute difference of cipher images D_{12} .

We further quantify differential behavior using NPCR (Number of Pixels Change Rate) and UACI (Unified Average Changing Intensity). The proposed algorithm achieves NPCR = 96.61% and UACI = 33.46%, which are competitive with recent methods (Table 4).

Table 4: NPCR and UACI Comparison

Algorithm	Proposed	Ref. [33]	Ref. [34]	Ref. [35]	Ref. [36]
NPCR (%)	96.61	99.63	99.61	99.60	99.60
UACI (%)	33.46	33.44	29.28	33.46	33.45

Overall, under the reported settings, the ciphertext exhibits near-uniform histograms, high entropy, low adjacent-pixel correlation, and competitive NPCR/UACI values, supporting strong statistical security characteristics.

7 Discussion

Deriving control parameters and initial conditions from a plaintext-dependent hash increases plaintext sensitivity and reduces key reuse across different images. This design also implies that encryption and decryption are tied to the exact plaintext representation; therefore, consistent preprocessing (e.g., file format and bit depth) is required for reproducibility.

The dominant computational cost arises from chaotic sequence generation, cross-channel bit operations, and the permutation–diffusion pass over all pixels. These operations are lightweight and can be optimized, but practical deployments should account for image-size scaling and platform constraints.

The evaluation in Section 6 follows widely used statistical tests and representative attack settings. Additional validation under alternative threat models and on larger, more diverse image sets would further strengthen the empirical evidence for robustness and practical applicability.

8 Conclusion

This paper presented an image-encryption algorithm driven by a hyperchaotic map derived from the proposed 3D-CCC structure. The scheme combines confusion and diffusion mechanisms guided by 3D chaotic dynamics, including (i) the 3D-CCC-based hyperchaotic construction, (ii) its use for parameter control and permutation, and (iii) a diffusion strategy driven by the generated sequences.

Experimental results indicate that the method achieves high entropy, low correlation, uniform histograms, and strong resistance to differential and brute-force tests under the reported settings. The key-space analysis further supports applicability to secure image transmission scenarios.

Relative to representative recent approaches, the proposed algorithm achieves competitive performance on the evaluated metrics, suggesting its practical potential for secure image storage, communication, and transmission.

Future work will consider computational optimization for real-time deployment and extensions to other multimedia formats beyond standard RGB images.

References

- [1] Ashish Singh, Kakali Chatterjee, Anish Kumar Singh, Neeraj Kumar, and Punam Prabha. Secure smart healthcare framework using lightweight dna sequence and chaos for mobile-edge computing. *IEEE Internet of Things Journal*, 10(6):4883–4890, 2022. doi:10.1109/JIOT.2022.3219113.
- [2] Suo Gao, Zheyi Zhang, Herbert Ho-Ching Iu, Siqi Ding, Jun Mou, Ugur Erkan, Abdurrahim Toktas, Qi Li, Chunpeng Wang, and Yinghong Cao. A parallel color image encryption algorithm based on a 2d logistic-rulkov neuron map. *IEEE Internet of Things Journal*, 12(11):18115–18124, 2025. doi:10.1109/JIOT.2025.3540097.
- [3] Yan Hong, Xinyan Duan, Jingming Su, Zhaopan Wang, and Shihui Fang. A novel approach to visual image encryption: 2d hyperchaos, variable josephus, and 3d diffusion. *Chinese Physics B*, 34(4):040504, 2025. doi:10.1088/1674-1056/adacc7.
- [4] Lizong Li. A novel chaotic map application in image encryption algorithm. *Expert Systems with Applications*, 218:124316, 2024. doi:10.1016/j.eswa.2023.124316.
- [5] Shaofang Wang, Jingguo Pan, Yanrong Cui, Zhongju Chen, and Wei Zhan. Fast color image encryption algorithm based on dna coding and multi-chaotic systems. *Mathematics*, 12(20):3297, 2024. doi:10.3390/math12203297.
- [6] E. Güvenoğlu. An image encryption algorithm based on multi-layered chaotic maps and its security analysis. *Connection Science*, 36:2312108, 2024. doi:10.1080/09540091.2024.2312108.
- [7] M. Zhao et al. A multi-image encryption scheme based on a new nd chaotic model and eight-base dna. *Chaos, Solitons & Fractals*, 187:115332, 2024. doi:10.1016/j.chaos.2024.115332.
- [8] Hangming Zhang, Hanping Hu, and Weiping Ding. Vsdhs-ciea: Color image encryption algorithm based on novel variable-structure discrete hyperchaotic system and cross-plane confusion strategy. *Information Sciences*, 665:120332, 2024. ISSN 0020-0255. doi:https://doi.org/10.1016/j.ins.2024.120332. URL https://www.sciencedirect.com/science/article/pii/S0020025524002457.
- [9] A. Yousefian Darani, Y. K. Yengejeh, H. Pakmanesh, and G. Navarro. Image encryption algorithm based on a new 3d chaotic system using cellular automata. *Chaos, Solitons & Fractals*, 179:114396, 2024. doi:10.1016/j.chaos.2023.114396.
- [10] Dilbag Singh, Sharanpreet Kaur, Mandeep Kaur, Surender Singh, Manjit Kaur, and Heung-No Lee. A systematic literature review on chaotic maps-based image security techniques. *Computer Science Review*, 54:100659, 2024. ISSN 1574-0137. doi:https://doi.org/10.1016/j.cosrev.2024.100659.
- [11] Dawei Ding, Haifei Zhu, Hongwei Zhang, Zongli Yang, and Dong Xie. An n -dimensional polynomial modulo chaotic map with controllable range of lyapunov exponents and its application in color image encryption. *Chaos, Solitons & Fractals*, 185:115168, 2024. doi:10.1016/j.chaos.2024.115168.

- [12] Shamsa Kanwal, Saba Inam, Shaha Al-Otaibi, Javaria Akbar, Nasir Siddiqui, and Muhammad Ashiq. An efficient image encryption algorithm using 3d-cyclic chebyshev map and elliptic curve. *Scientific Reports*, 14(1):29626, 2024. doi:10.1038/s41598-024-77955-w.
- [13] Khalid M. Hosny, Yasmin M. Elnabawy, Rania A. Salama, and Ahmed M. Elshewey. Multiple image encryption algorithm using channel randomization and multiple chaotic maps. *Scientific Reports*, 14(1):30597, 2024. doi:10.1038/s41598-024-79282-6.
- [14] Chunyun Xu, Yubao Shang, Yongwei Yang, and Chengye Zou. An encryption algorithm for multiple medical images based on a novel chaotic system and an odd-even separation strategy. *Scientific Reports*, 15(1):2863, 2025. doi:10.1038/s41598-025-86771-9.
- [15] Di He, Chuan He, Liguang Jiang, Huiwei Zhu, and Guorong Hu. A chaotic map with infinite collapses. In *2000 TENCON Proceedings. Intelligent Systems and Technologies for the New Millennium (Cat. No. 00CH37119)*, Vol. 3, pages 95–99. IEEE, September 2000.
- [16] Shashikant C. Phatak and S. Suresh Rao. Logistic map: A possible random-number generator. *Physical Review E*, 51(4):3670–3673, 1995. doi:10.1103/PhysRevE.51.3670.
- [17] Jory Griffin. The sine map. <https://www.jorygriffin.com/sine-map/>, 2013. Accessed: 2018-05-04.
- [18] Qing He, Peng Li, and Yucheng Wang. A color image encryption algorithm based on compressive sensing and block-based dna coding. *IEEE Access*, 12:77621–77638, May 2024. doi:10.1109/ACCESS.2024.2375972.
- [19] Cheng Wang, Zhong Chong, Hong Zhang, Peng Ma, and Wei Dong. Color image encryption based on discrete memristor logistic map and dna encoding. *Integration*, 96:102138, May 2024. doi:10.1016/j.vlsi.2023.102138.
- [20] Tian Zhang and Sheng Wang. Image encryption scheme based on a controlled zigzag transform and bit-level encryption under the quantum walk. *Frontiers in Physics*, 10:1097754, January 2023. doi:10.3389/fphy.2022.1097754.
- [21] Zhen Liang, Qian Qin, Chao Zhou, and Shiqi Xu. Color image encryption algorithm based on four-dimensional multi-stable hyper chaotic system and dna strand displacement. *Journal of Electrical Engineering & Technology*, 18(1):539–559, January 2023. doi:10.1007/s42835-022-01114-9.
- [22] Daniel E. Mfungo and Xiang Fu. Fractal-based hybrid cryptosystem: Enhancing image encryption with rsa, homomorphic encryption, and chaotic maps. *Entropy*, 25(11):1478, October 2023. doi:10.3390/e25111478.
- [23] Manoj Kar, Anil Kumar, Debi Prasad Nandi, and Manas Kumar Mandal. Image encryption using dna coding and hyperchaotic system. *IETE Technical Review*, 37(1):12–23, January 2020. doi:10.1080/02564602.2018.1524899.
- [24] Xingyuan Wang and Ning Guan. 2d sine-logistic-tent-coupling map for image encryption. *Journal of Ambient Intelligence and Humanized Computing*, 14(10):13399–13419, October 2023. doi:10.1007/s12652-022-04704-1.
- [25] Qing Lu, Linlan Yu, and Congxu Zhu. Symmetric image encryption algorithm based on a new product trigonometric chaotic map. *Symmetry*, 14(2):373, 2022. doi:10.3390/sym14020373.
- [26] Narbda Rani, Vinod Mishra, and Suvita Rani Sharma. Image encryption model based on novel magic square with differential encoding and chaotic map. *Nonlinear Dynamics*, 111(3):2869–2893, 2023. doi:10.1007/s11071-022-08194-0.
- [27] Heping Wen et al. Exploring the future application of uavs: Face image privacy protection scheme based on chaos and dna cryptography. *Journal of King Saud University - Computer and Information Sciences*, 36(1):101871, 2024. doi:10.1016/j.jksuci.2023.101871.
- [28] Manzoor Ahmad Lone and Shaima Qureshi. Encryption scheme for rgb images using chaos and affine hill cipher technique. *Nonlinear Dynamics*, 111(6):5919–5939, 2023. doi:10.1007/s11071-023-08593-x.
- [29] B. Ahuja and R. Doriya. A secure algorithm using high-dimensional sine map for color image encryption. *International Journal of Information Technology*, 15(3):1535–1543, 2023. doi:10.1007/s41870-022-01078-0.
- [30] Xingyuan Wang et al. An image encryption scheme using bit-plane cross-diffusion and spatiotemporal chaos system with nonlinear perturbation. *Soft Computing*, 27(3):1223–1240, 2023. doi:10.1007/s00500-022-07868-x.
- [31] Muhammad Imran Haider et al. An innovative approach towards image encryption by using novel prns and s-boxes modeling techniques. *Mathematics and Computers in Simulation*, 209:153–168, 2023. doi:10.1016/j.matcom.2023.03.018.
- [32] Guodong Ye et al. Image encryption scheme based on blind signature and an improved lorenz system. *Expert Systems with Applications*, 205:117709, 2022. doi:10.1016/j.eswa.2022.117709.

- [33] Shuqin Zhu and Congxu Zhu. A visual security multi-key selection image encryption algorithm based on a new four-dimensional chaos and compressed sensing. *Scientific Reports*, 14(1):15496, 2024. doi:10.1038/s41598-024-70445-5.
- [34] Huda Rashid Shakir, Sadiq Abdul Aziz Mehdi, and Anwar Abbas Hattab. Chaotic-dna system for efficient image encryption. *Bulletin of Electrical Engineering and Informatics*, 11(5):2645–2656, 2022. doi:10.11591/eei.v11i5.3674.
- [35] Hui Wang et al. A novel image shift encryption algorithm based on the dynamic joseph ring problem. *Multimedia Tools and Applications*, 82(26):39897–39927, 2023. doi:10.1007/s11042-023-15466-x.
- [36] Geeta Biban, Renu Chugh, and Anju Panwar. Image encryption based on 8d hyperchaotic system using fibonacci q-matrix. *Chaos, Solitons & Fractals*, 170:113396, 2023. doi:10.1016/j.chaos.2023.113396.